# Real-Time Detection of Cavitation for Hydraulic Turbomachines

Cavitation is an important problem in hydraulic machines that negatively affects their performance and may cause damages. Image processing techniques have been often used for visual analysis of cavitation conditions. Real-time detection of cavitation inception is more critical. This is usually performed by measuring related vibrations or electrical impedance, but coarse errors occur. Even if vision inspection is one of the first methods to analyse cavitation damages, this paper presents an innovative approach, i.e. a vision-based system for real-time detection of cavitation inception. Experimental results in real conditions are reported, which were obtained by testing the system proposed. This technique can be applied to any hydraulic turbomachine, provided that an optical access is available.

© 1998 Academic Press

**Antonio Baldassarre[1], Maurizio De Lucia[1] and Paolo Nesi[2]**

[1]*Department of Energy Engineering,*
*University of Florence, Via di Santa Marta, 3, 50139 Firenze, Italy*
[2]*Department of Systems and Informatics,*
*University of Florence, Via di Santa Marta, 3, 50139 Firenze, Italy*

## Introduction

Cavitation is an important and unpleasant phenomenon which may occur along stationary parts of hydraulic machines and/or along moving blades, as in centrifugal pump impellers [1]. This occurs when, due to a decrease in local pressure up to the vapor pressure, cavities filled with water vapor are formed. These cavities grow particularly on the impeller blade, where there exists the lowest pressure value, and they tend to increase in size and to be dragged out by the fluid flow. As soon as the vapor bubbles reach regions of higher pressure on their path through the centrifugal pump they collapse by an implosion, producing the whirlpool of the liquid of the neighboring zone (Figure 1). For phenomenological and thermodynamics studies of cavitation, please refer to Stepanof [1], Franc *et al*. [2], Sulzer Brothers Ltd. [3] and Lobanoff and Ross [4].

Strong cavitation phenomena are usually manifested by some signs, all of which negatively affect the pump performance and can even damage pump parts. Noise and vibration are external detectable signs of cavitation which are caused by the sudden collapse of vapor bubbles. Another sign is the strong decrease in pump efficiency, due to the reduction of its capacity. Moreover, if a pump operates under cavitation conditions for a sufficient interval of time, a rapid erosion of blade surfaces (usually named pitting) occurs. This must be avoided, since damages are not reversible. The amount of metal loss depends on the impeller material and on the degree of cavitation. It was shown by Foettinger [5], that blade pitting is caused solely by the mechanical action of collapsing vapor bubbles, and that electrolytic and chemical actions are substantially insignificant in the cavitation phenomenon. Therefore, erosion is caused by very strong local values of pressure (water-hammer). Additional comments on the various undesirable phenomena related to cavitation (noise, presence of bubbles, erosion, pressure fluctuations, etc.), and their implications on industrial machines are reported by Canavelis and Grison [6]. A study of close interactions
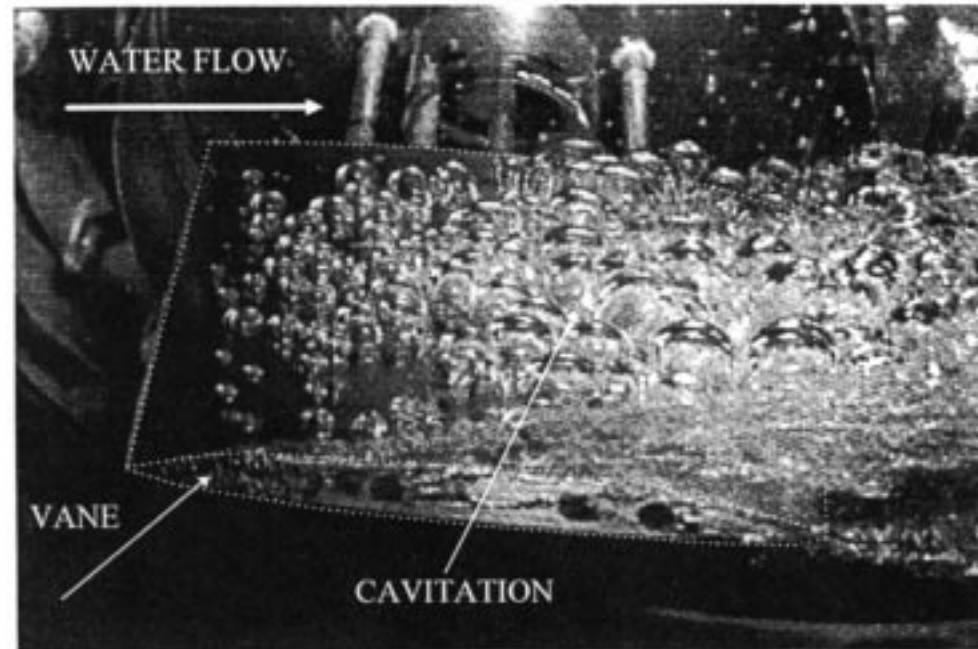
**Figure 1.** Fluid flow on a blade under cavitation (extracted from Franc *et al*. [2]).

between fluid mechanics, cavitation and erosion effects has been presented in the work of Durrer [7].

The phenomenon of cavitation presents two aspects: (i) the need for early detection of cavitation, and (ii) the analysis of cavitation conditions. The early detection of cavitation can be used to avoid damages which change the operating conditions, and thus cause an uncontrolled decrease in pump performance. Due to the high velocity of cavitation inception phenomena, different techniques for cavitation detection in real-time have been often proposed. For example, by considering that cavitation in hydraulic machines is always associated with vibration and noise, having features and intensity depending on the cavitation conditions, some methods based on acoustic investigations have been presented in Varga [8]. Two methods for detecting bubbles in a fluid have been compared in Ceccio [9]: the former being based on acoustic emission, and the latter on changes in electrical impedance. Acoustic methods are too sensitive to noise, since they are based on measuring vibration in a strongly noisy environment. Usually the cavitation main frequency is characterized by values higher than that coming from other mechanical parts. Acoustic methods are not capable of distinguishing cavitation from noise and vibrations due to other cavitating components; thus, their threshold for detecting cavitation inception must be higher than noise/vibration, and they are not sensitive enough. Analogous problems and a similar performance have been observed for methods based on electrical

impedance. Therefore, both techniques are only suitable for detecting macroscopic cavitation [9].

In general, both intrusive and non-intrusive flow visualization techniques have been adopted for studying fluid dynamics. However, in the study of the cavitation phenomenon flow visualization techniques have an important role, particularly in the analysis of cavitation conditions. This means that, in many cases, once the cavitation inception is detected, it can be very useful to analyse an image of the phenomenon for evaluating in depth the characteristics of cavitation (see, for example, Merzkirsch [10] and Yang [11]). Most of these are only qualitative studies of the cavitation phenomenon, and frequently they are supported by human analysis of static images. The concept of cavity length and extension, measured by visual inspection or directly by photo sequences, has become a standard method for evaluating cavitation conditions. These have been related to the cavitation erosion rate on the basis of a large amount of experimental data, thus making it possible to predict major machinery damages and faults [6,12–14]. An investigation of the influence of cavity length on erosion and lack of performance was also carried out by Stoffel [15]. Some experiments on automatic analysis of cavitation zones by means of image processing have been presented by De Lucia [16]. The most diffuse technique for taking single snapshots of cavitation on each blade is to employ a stroboscopic or a laser light synchronized with pump impellers and a TV camera.

As a conclusion, several authors in the literature have adopted image processing techniques to study and to characterize cavitation, but not to develop a real-time system for cavitation detection. For such an application, "real-time" means fast enough to avoid the pump impeller erosion and to control the machine performance in the context of the system in which the pump is used. The system presented has a slow control loop which reads the system sensors and produces the controlled outputs 10 times per second.

In this paper, an image processing system for real-time detection of cavitation inception is proposed. The main goal is to produce an alarm signal indicating in real-time the occurrence of cavitation. To this end, three different algorithms have been defined, implemented and compared in real conditions. Experiments have been performed on a GE-Nuovo Pignone centrifugal pump. The approaches proposed are capable of producing results from which cavity length and extension can be directly evaluated, and used as a basis for the algorithms defined by one of the authors [16]. In the next sections, after a description of the system overview, the algorithms for cavitation detection are presented. Some aspects of the real-time implementation are also reported. Finally, the typical results produced by the experiments performed are presented, showing the differences among the algorithms proposed.

## System Overview

Experiments on cavitation inception and evolution have been carried out on a single-section, double-volute centrifugal pump with a specific speed $N_s = 28.8$ (m$^3$/s, m, rpm) and a capacity coefficient $\phi = 0.126$. This pump is manufactured by Nuovo Pignone, Italy, for high pressure and temperature applications. The centrifugal pump has been extensively tested on the pump-test facility of the Department of Energy Engineering of the University of Florence. The pump-test facility is driven by a 250 kW DC-motor and its performance and operating conditions are described by Arnone *et al.* [17]. The pump under test has six blades on a diameter of 235 mm, and its operating conditions are 1100 m$^3$/h at 1500 rpm. In order to guarantee the correct detection of cavitation the fluid must be clear, even if some contaminations due to the presence of particles are supported.

In order to make the cavitation flow visible, a clear Plexiglas tube, which exactly reproduced the original tube shape, was placed at the inlet side. The design of the transparent tube was particularly critical, since this strongly
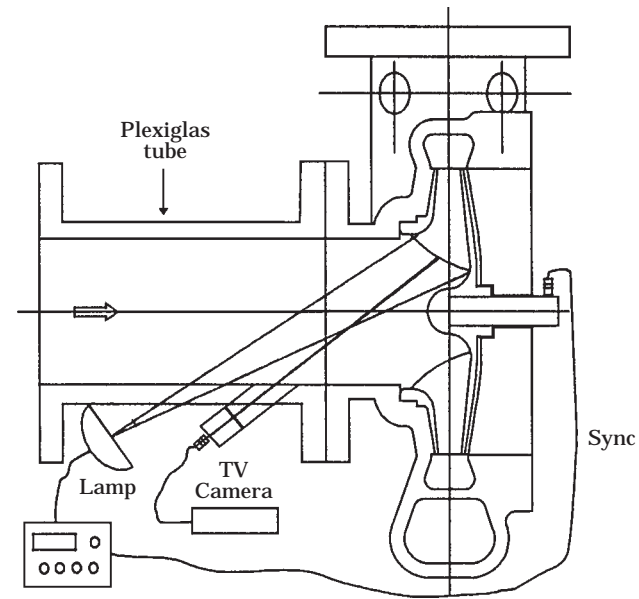


**Figure 2.** Sketch of the mechanical system and image acquisition section.

influences the image quality. In fact, quality and sharpness of images are relevant for the success of some of the following image processing steps, as it will be highlighted later. The tube supports a small video camera mounted on the inlet side (Figure 2), in order to view the frontal part of the pump impeller.

The video camera has been placed so as to focus closely on the target blade without interfering with the inlet flow. In order to obtain high-quality images, the layout of the system was conceived to achieve the intensity and quality of lighting needed – i.e. without reflections or shadows by other objects.

Figure 3 shows the system overview. The TV camera (Sony CCD video camera module XC-77RR-CE, 756 × 581 pixels) can grab image frames on the basis of an external synchronization. The acquisition board (Matrix Board, 768 × 512 pixels, endowed with external sync) digitizes images from the TV camera. The acquisition board is directly connected with the PC (i486 DX2 66 MHz), which can process images in real time. In this system, a couple of monitors have been used to control the video signals coming from the TV camera and the image acquisition board, Video and Video Live, respectively.

In order to guarantee the stability of acquired frames (grabbing the selected blade in the same position at each time instant) in spite of the high speed of the pump impeller
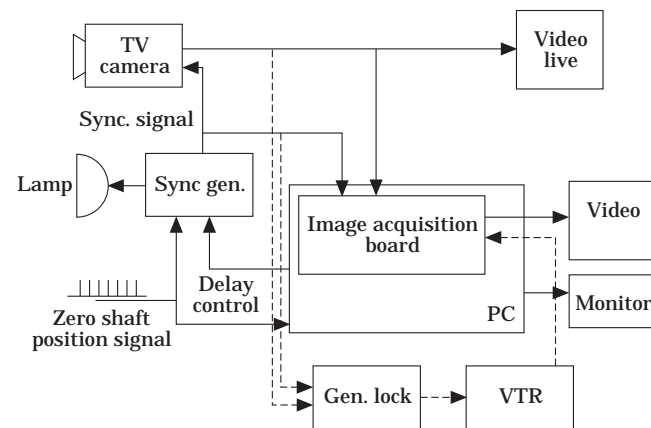
**Figure 3.** System overview.



**Figure 4.** Timing of synchronization signals.

and the turbulent nature of bubbles, a very short shutter time for the TV camera has been used. The lighting system has been implemented by using a stroboscopic lamp to produce an intense light only during camera sampling. This avoids a temperature increase due to the high power needed to illuminate the blade as required by the small acquisition time of the TV camera. The stroboscopic lamp and the video-camera shutter have been driven by an *ad hoc* signal synchronization generator (SyncGen in Figure 3). This synchronizes the TV camera, the frame grabber and the stroboscopic lamp. By controlling the zero shaft position signal and producing the delay time, it is possible to select the periodic sampling of a specific impeller blade. As depicted in Figure 3, when the shaft reaches the zero reference position a pulse is sent to the SyncGen. After a programmable delay SyncGen generates a command for the lamp and the camera shutter. SyncGen also allows to select the blade under analysis by introducing a programmable delay, as shown in Figures 3 and 4. When the rotational speed changes, the value of delay must be adjusted according to the speed measured by means of zero shaft position signal. Frames grabbed during speed adjusting are neglected.

Please note that, as reported in Figure 3, a video recorder (VTR Betamax, Sony UVW-l400AP) has been adopted for our experiments in order to reproduce the same test conditions several times for testing different algorithms and parameters. To this end, the signal coming from the camera has been rec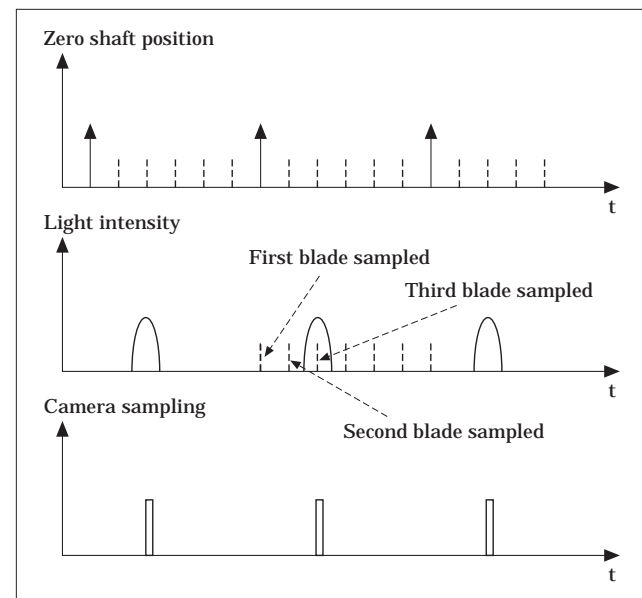onstructed by a Genlock to adapt the non-standard frame frequency produced by the TV camera, and constrained by the speed of the impeller to that of the VTR which uses PAL as the broadcasting standard.

## Cavitation Detection Algorithms

As was already pointed out, the main goal of our system is to detect in real time the inception of cavitation. To this end, a vision-based system has been built; thus, an image presenting a single blade can be grabbed at selected time instants. Figure 5 shows four acquired frames of an impeller blade under different cavitation conditions: (a) without cavitation, (b) incipient cavitation, (c) and (d) during the increase in cavitation. As can be observed in Figure 5, the cavitation is highlighted by a clearer region with respect to the non-cavitated conditions. This is due to the fact that the surface of a formed bubble separates two different optical media, liquid water and water vapor; the light reaching the bubble surface is partially reflected, and thus the bubbles appear brighter. Therefore, on the basis of the previously described image acquisition architecture, when cavitation occurs a zone, named the *cavitation zone*, appears where the brightness of image pixels increases and changes in intensity very rapidly over time – i.e. the phenomenon is turbulent.

According to the needs of the real-time response, three different algorithms for detecting cavitation inception have
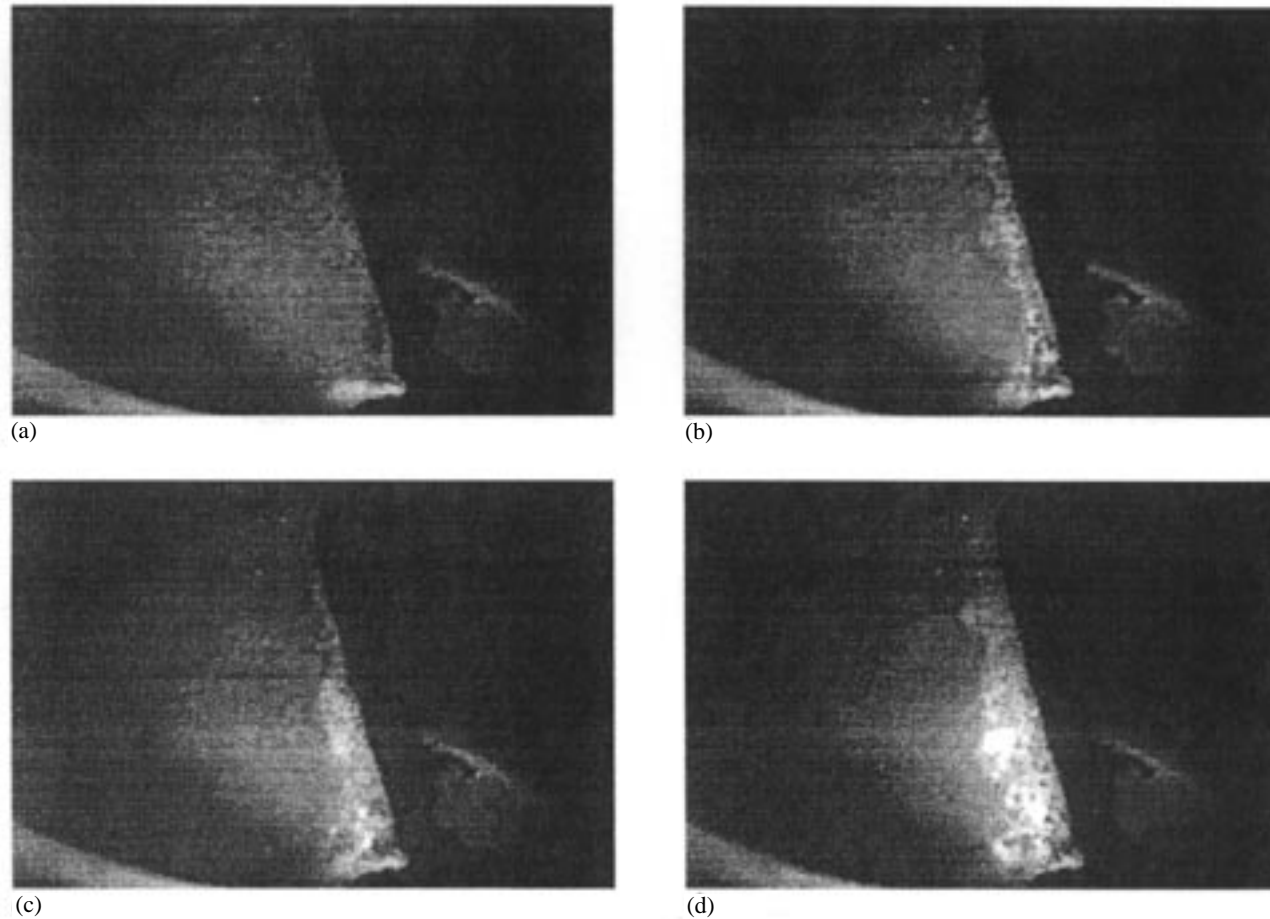
**Figure 5.** Impeller blade under conditions of: (a) no cavitation; (b) incipient cavitation; and (c), (d) increasing cavitation (acquired by our system).

been defined and tested. In the following, these algorithms are reported in the order in which they were defined.

In the rest of this paper, images are expressed in terms of their pixels whose values represent the image brightness, $E(x, y, t)$, the ratio between the infinitesimal power lighting an infinitesimal surface extending around point $P(x, y)$ at time $t$, and the area of the infinitesimal surface [18]. For the system described each pixel is represented by 8 bits: 0 (black)–255 (white)

*First algorithm*

The first method is based on the assumption that a pixel is in the *cavitation zone* if its image brightness is greater than a given threshold $th_a$. Therefore, the inception of cavitation can be detected by counting the number of pixels in those conditions. This extremely simple approach is affected by several drawbacks. The most important problem is due to

the fact that the analysis of the whole image is too heavy to be performed in real time with low-cost and non-custom architecture. For this reason, image processing must be limited to a region of interest (ROI). This region must obviously be identified before algorithm execution. This is not a limitation, since the specific blade profile of the centrifugal pump is known. Therefore, let us now assume that the ROI, $\Gamma$, is known. By using the ROI, $\Gamma$, as a reference, a set of image pixels can be selected from the image under analysis at time $t$, saving in this way the time for processing the whole image:

$$\psi(E, \Gamma, t) = \{E(P(x, y), t) \mid P(x, y) \in \Gamma\}$$

On this set, only pixels having a value higher than a given threshold are selected by:

$$A_a(\psi, th_a) = \{P(x, y) \mid E(P(x, y), t) \in \psi(E, \Gamma, t) \wedge E(P(x, y), t) > th_a\}$$

The number of the elements of this set, $f_a(t)$, is considered as a measure of cavitation magnitude:

$$f_a(t) = misure(A_a(\psi, th_a), t)$$

On the other hand, this measure is usually affected by coarse errors due to noise and to the fact that the 3D profile of blades has different brightness values in different points of the blade surface. Too small a value for the threshold $th_a$ leads to the counting also of brighter impeller pixels where cavitation is absent. These problems can be partially solved by selecting a suitable threshold $th_a$, as discussed in the following.

On the basis of the above measure, a detection signal which states the blade condition – i.e. cavitation or normal –- is defined as a binary function:

$$d_a(t) = \begin{cases} cavitation & \text{if } f_a(t) > td_a \\ normal & \text{otherwise} \end{cases}$$

where $td_a$ is a threshold used for detecting cavitation inception from cavitation magnitude.

With this algorithm, the problems due to the non-uniformity of brightness of the blade are not solved. In fact, with this method a bubble may not be detected when it occurs, but only if its brightness rises over the predefined value. During cavitation, if an area of the blade is too dark, a bubble does not reach the predefined value of brightness, and consequently it is not detected. In addition, some blades can have a given pattern due to previous erosions which can cause an additional unpredictable noise. For the same reason, this algorithm is quite sensitive with respect to changes in image brightness, which can be due to changes in fluid transparency and light intensity. This problem is avoided by using a stroboscopic light with a constant intensity. In order to solve the above discussed problems, the following algorithms have been defined.

*Second algorithm*

This algorithm is based on the assumption that bubbles can grow at different depths (with respect to the TV camera blade direction) and from blade areas at a different brightness. Therefore, a pixel is considered to be in the cavitation zone if its value is changed with respect to the corresponding value before the occurrence of cavitation. Hence, the analysis is based on the difference in the image brightness of each blade pixel and not on its value; thus reducing problems related to changes in image brightness. To this end, a reference set of image pixels is extracted in the initialization phase by using the ROI, $\Gamma$, in the absence of cavitation:

$$\psi_r(E_r, \Gamma, t_r) = \{E_r(P(x, y), t_r) \mid P(x, y) \in \Gamma\}$$

Then the set of pixels under cavitation is described as:

$$\begin{aligned} A_b(\psi, \psi_r, th_b) = \\ \{P(x, y) \mid E(P(x, y), t) \in \psi(E, \Gamma, t) \wedge E_r(P(x, y), t_r) \\ \in \psi_r(E_r, \Gamma, t) \wedge \mid E(P(x, y), t) - E_r(P(x, y), t_r) \mid < th_b\} \end{aligned}$$

The number of elements of this set, $f_b(t)$, is used to evaluate the cavitation magnitude:

$$f_b(t) = misure(A_b(\psi, \psi_r, th_b), t)$$

Also, in this case, $f_b(t)$ is usually affected by errors due to noise. Too small a threshold value may also lead to the consideration of noise as cavitated points.

On the basis of the cavitation magnitude, the detection signal $d_b(t)$ is defined as a binary function of threshold $td_b$, as performed for the previous algorithm.

Both the first and second algorithms can be considered as quite good criteria for detecting the inception of cavitation, if suitable $th$ and $td$ thresholds are chosen. These can be evaluated on the basis of a few measures in the absence of cavitation by using the same image acquisition system as discussed in the sequel. On the other hand, both of the above algorithms are much too sensitive with respect to the intrinsic stochastic nature of cavitation. This phenomenon produces a high-frequency component during cavitation, and thus this effect is reflected in both $f_a(t)$ and $f_b(t)$, and sometimes also in $d_a(t)$ and $d_b(t)$. This problem can be strongly reduced by using suitable filters on the cavitation magnitude as a function of time, as discussed in the following. The sets of pixels $A_a(\psi, th_a)$ and $A_b(\psi, \psi_r, th_b)$, which identify the cavitated region, are non-uniformly composed of pixels due to cavitation conditions. This can be a problem if the image representing the sets should be used in a successive phase of analysis in which, for example, the area of the region must be measured. In order to solve this problem the following algorithm has been defined.

*Third algorithm*

Problems which are present on the previously described algorithms are mainly due to the high frequency component of cavitation. In order to reduce these effects, the set of pixels on which the measure is performed can be differently
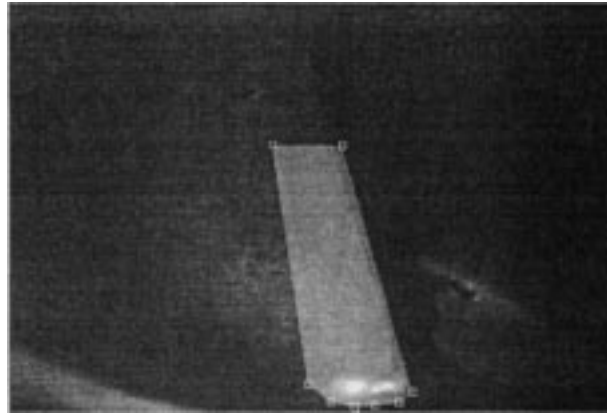
**Figure 6.** Impeller zone under analysis (ROI) of 27 762 pixels, subimage extracted by a $768 \times 512$ image.

defined. To this end, the analysis of cavitation detection has been performed by considering a temporal window instead of only the last image. In particular, in this algorithm, pixels belonging to set $A_c(\psi, \psi_r, th_b)$ are considered; this set is evaluated as the union of sets $A_b(\psi, \psi_r, th_b)$ in the temporal window selected:

$$A_c(\psi, \psi_r, th_b) = \bigcup_{t-(n-1)\Delta t}^{t} A_b(\psi, \psi_r, th_b).$$

This means that a pixel is considered to be in the cavitation zone if it has been found to be cavitated at least once in the temporal window. This mechanism performs a sort of low-pass filtering directly in the identification of the pixels under cavitation. The dimension of the time interval must be selected for trimming the high-frequency components, by heuristic analysis or by using a frequency analysis of cavitation magnitude. Therefore, even in this case the cavitation magnitude is defined as:

$$f_c(t) = misure(A_c(\psi, \psi_r, th_b), t)$$

Unfortunately, even in this case $f_c(t)$ can be affected by errors due to noise. The detection signal $d_c(t)$ has been defined as a binary function of threshold $td_c$.

## Algorithm Implementation and Experimental Results

Our experiments have been carried out by reproducing the actual operating conditions of the centrifugal pump. Cavitation conditions have been produced by controlling the inlet and outlet valves so as to lower the inlet pressure, while maintaining the stability of the flow rate and the rota-
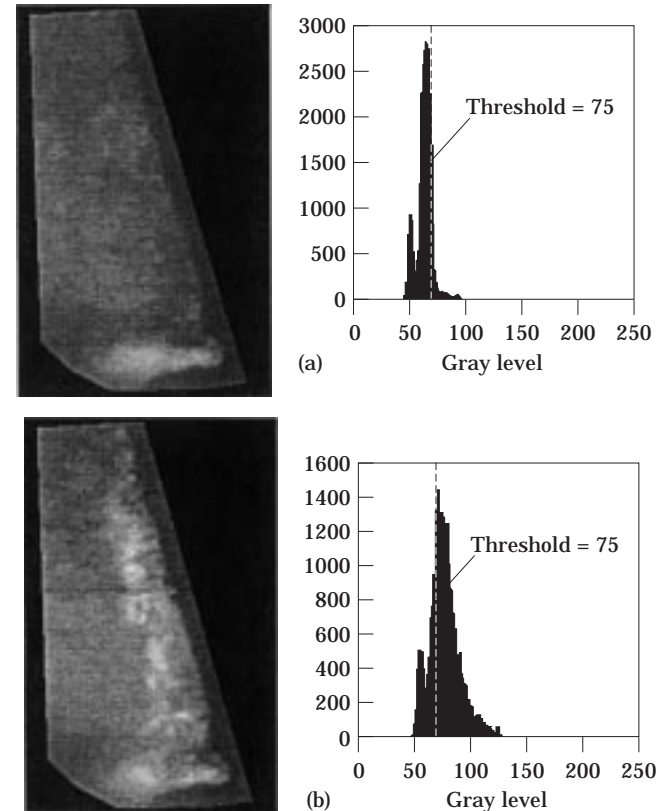


**Figure 7.** Impeller zone under analysis and relative histogram (first algorithm): (a) before cavitation, (b) during cavitation.

tional speed, since this is what usually occurs in real conditions. Near the inlet section of the pump impeller the measure of the inlet flow conditions was performed with four static taps. For the outlet the measure at the exit of the volute was obtained with eight static taps.

Each experiment was started in the absence of cavitation and was carried out for about 4 min. Cavitation inception was caused after about 35 s by adjusting the inlet and outlet valves so as to lower the inlet pressure. Cavitation was also further increased after about 130 s.

In general, the processing procedures resulting from the algorithms described can be regarded as composed of four steps: (i) selecting the blade; (ii) choosing the ROI on the impeller; (iii) imposing suitable values for thresholds $th$ and $td$ on the basis of the selected algorithm; and (iv) loop acquiring and monitoring.

According to Figure 5, the straight line of the leading edge can be used to define a limit of the impeller zone under analysis, ROI, as depicted in Figure 6.

In fact, cavitation inception occurs close to the leading edge, extending its influence in a limited region on the blade (on the left of the edge); thus, the algorithms were based on a limited region to improve their performance.

Experiments on the three algorithms were carried out by using several image sequences in real time in order to verify their capabilities for detecting cavitation conditions. Some typical image sequences were also stored on an analog support to compare the algorithm performance on the basis of the same image sequences. Each algorithm produces the cavitation magnitude and the detection signals as a function of time. The cavitation magnitude is strongly sensitive to noise and high-frequency components of cavitation, which in turn were attenuated by using filters.

*Experiments based on the first algorithm*

According to the first algorithm and on the basis of the ROI, $\Gamma$, a $\psi(E, \Gamma, t)$ is evaluated at each time instant. This process is performed by scanning the ROI row by row, and evaluating at the same time the measure $f_a(t)$ of set $A_a(\psi, th_a)$. This allows $f_a(t)$ to be obtained in a unique scan of ROI, which implies access to the directly related pixels.

The critical phase of this algorithm is the identification of the threshold; this must be performed on the basis on the operating conditions – light, blade selected, ROI etc. To this end, an automatic preliminary phase for evaluating the threshold was implemented. In this phase, the ROI is extracted in the absence of cavitation (Figure 7(a)).

The histogram presents two main spikes; the former is due to the background gray level (the first on the left), and the latter to the blade surface (the highest spike). Moreover, a very small spike due to the presence of blade connection with its support is also present. On these bases the threshold is selected by trimming the main spikes and including the small spike due to the blade connection, as reported in Figure 7(a). The small spike was excluded, since the cavitation produces a spike close to that value. The small spike leads to an offset value for the cavitation magnitude, $f_a(t)$. In general, this offset and function $f_a(t)$ also present a small noise, as discussed in the following.

In Figure (7b) the histogram obtained in the presence of cavitation is reported. It can be noted that the spike due to the background gray level is still present, while the cavitation zone is quite over the selected threshold. The classical identification of threshold, frequently adopted for bimodal histograms [18] – i.e., choosing $th_a$ on the basis of the
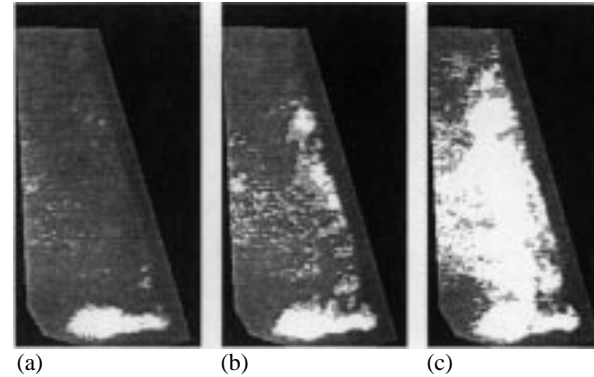


(a)           (b)           (c)

**Figure 8.** $A_a(\psi, th_a)$ set on frame during: (a) absence of cavitation ($t = 15$ s), (b) cavitation ($t = 75$ s), (c) strong cavitation ($t = 170$ s).

minimum value between spikes – is not suitable in this case, since we are interested in detecting cavitation and not in selecting its area when the cavitation covers the whole ROI. On the contrary, the method chosen guarantees a high sensitivity to cavitation detection (number of pixels).

The asymptotic complexity of this first algorithm is $O(R)$, where $R$ is the ROI dimension.

Figure 8 shows some typical frames where set $A_a(\psi, th_a)$ is highlighted. They have been acquired during: (a) absence of cavitation ($t = 15$ s), (b) cavitation ($t = 75$ s), (c) strong cavitation ($t = 75$ s).

Figure 9 shows the value of the cavitation magnitude as a function of time during the experiment obtained by the first algorithm in the three different conditions by using $th_a = 70$. By observing the trend of cavitation magnitude, it is quite evident that the selection of a suitable threshold $td_a$ without filtering and by using a median filter is quite difficult (many spikes and glitches are present), and low levels of cavitation are usually missed. When the mean filtering was adopted, an easier identification of $td_a$ was possible. Median and mean filters were selected for their low computational cost with respect to more sophisticated filters. In the diagrams reported, median and mean filtering was performed on 16 samples.

*Experiments based on the second algorithm*

According to the second algorithm and on the basis of the ROI, a reference $\psi_r(E_r, \Gamma, t_r)$ is evaluated at the beginning of the process, while $\psi(E, \Gamma, t)$ is evaluated at each time instant. This is performed by scanning the ROI row by row, and evaluating at the same time the measure of set $A_b(\psi, \psi_r, th_b)$. This allows to obtain $f_b(t)$ with a unique scan of the ROI.
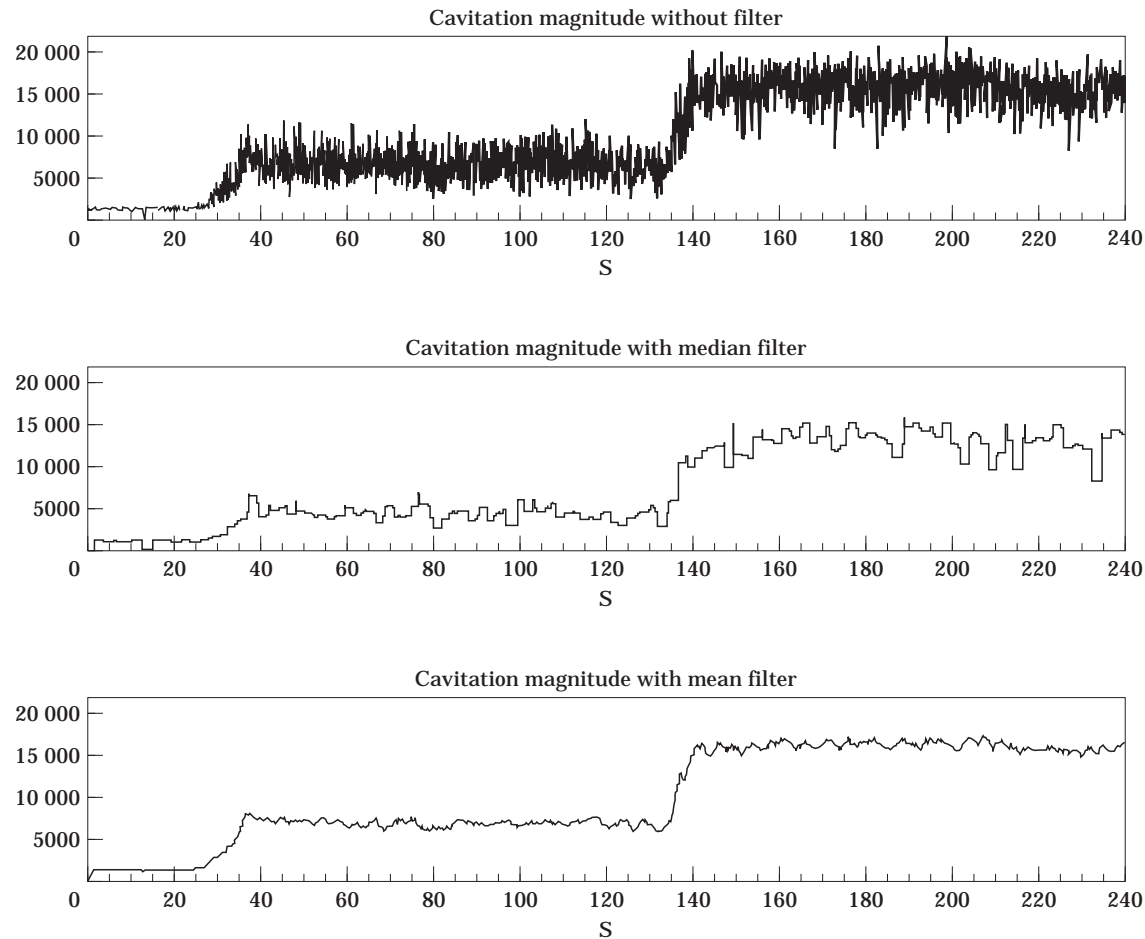
Cavitation magnitude without filter

Cavitation magnitude with median filter

Cavitation magnitude with mean filter

**Figure 9.** Cavitation magnitude as a function of time, obtained by using the first algorithm.

The critical phase is the identification of the threshold, but an automatic preliminary phase for evaluating threshold $th_b$ has been defined. In this case, the histogram is evaluated on the image which is the difference in brightness between an actual frame and $\psi_r(E_r, \Gamma, t_r)$. The presence of a difference between images leads to the traditional problems of misalignment. These are very small on the blade (for its smooth brightness), while on the leading edge they can produce coarse errors due to the shadowed zone. This problem can be avoided by selecting a ROI which does intersect the leading edge.

The ROI histogram extracted in the absence of cavitation is presented in Figure 10(a). In this case, the histogram of image difference presents only one peak due to the variability of image brightness. The threshold is selected by trimming the peak, as reported in Figure 10(a). The absence of a small peak leads to the lack of an offset value for the detection function $f_b(t)$.

In Figure 10(b) the histogram obtained in the presence of cavitation is reported. It can be noted that it still presents only one peak with a larger base due to the cavitation zone; please note that the scale in these histograms is different. Thus, the method chosen guarantees a good sensitivity of cavitation detection (Figure 10(b)).

The asymptotic complexity of this second algorithm is $O(R)$, where $R$ is the ROI dimension.

Figure 11 shows some sample frames where the set $A_b(\psi, \psi_r, th_b)$ is highlighted. These have been acquired during: (a) absence of cavitation ($t = 15$ s), (b) cavitation ($t = 75$ s), (c) strong cavitation ($t = 75$ s).

Figure 12 shows the value of the cavitation magnitude as a function of time during the experiment obtained for three different conditions by using a threshold $th_b = 10$. In this case, a quite reliable detection signal can be evaluated only on the filtered cavitation magnitude signal.
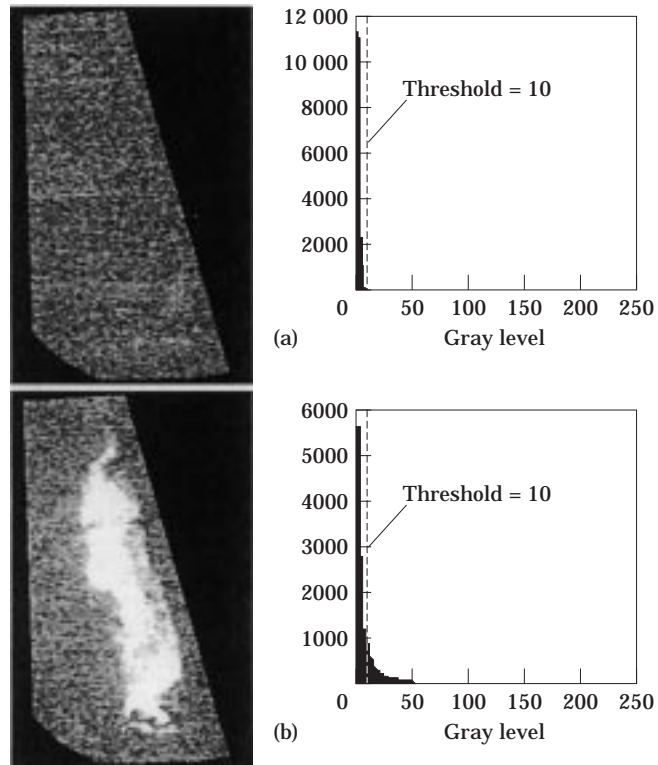
**Figure 10.** Image difference between a frame and a template and the relative histogram (second algorithm): (a) before cavitation and (b) during cavitation.



**Figure 11.** $A_b(\psi, \psi_r, th_b)$ set on frame during: (a) absence of cavitation ($t = 15$ s), (b) cavitation ($t = 75$ s), (c) strong cavitation ($t = 170$ s).

*Experiments based on the third algorithm*

According to the second algorithm, the set $A_b(\psi, \psi_r, th_b)$ is evaluated at each time instant. For each pixel of the ROI a FIFO structure having dimension equal to the temporal window is provided. This FIFO is used to memorize the behavior of the ROI pixels in belonging or not to the set $A_b(\psi, \psi_r, th_b)$. At each time instant, the overall FIFO structure is updated by analysing each pixel of the ROI, thus pushing 1 for pixels in the presence of cavitation and 0 otherwise, according to the second algorithm. The FIFO structure is updated at the same time as the evaluation of cavitation magnitude. The magnitude is evaluated by considering as cavitated the pixels having at least a 1 in the FIFO. Changing the dimension of the temporal window increases the asymptotically complexity, which is an $O(R\,W)$, where $R$ is the ROI dimension and $W$ is the dimension of the FIFO. Please note that since the FIFO is implemented by using data types available in the microprocessor (byte, word, double word), it assumes discrete values: 8, 16, 32, etc. Total algorithm costs are different due to cost differences in detecting a non-zero value in the FIFO and shifting the FIFO. Both these operations can be performed in a number of cycles, which usually are dependent on the register dimension.
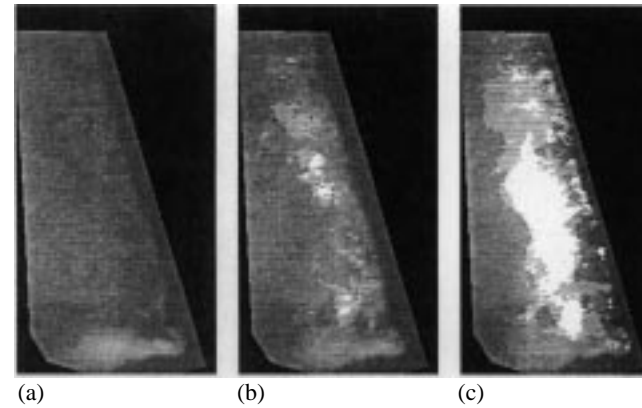
Figure 13 shows sample frames where the set $A_c(\psi, \psi_r, th_c)$ is highlighted. These have been acquired during: (a) absence of cavitation ($t = 15$ s), (b) cavitation ($t = 75$ s), (c) strong cavitation ($t = 75$ s).

Figure 14 shows the behavior of cavitation magnitude as a function of time which was obtained in three different conditions using a threshold $th_c = 10$. In this case, the threshold for obtaining the detection signal can be applied even on the non-filtered cavitation magnitude, producing reliable and stable results.

## Algorithm Comparison

The results obtained for the cavitation magnitude as a function of time for the algorithms proposed show that the first algorithm presents the lowest sensitivity to cavitation conditions. This is mainly due to the presence of an evident offset. This behavior is also confirmed by the frequency analysis reported in Figures 15 and 16.

The accurate comparison of the algorithms has pointed out that the cavitation magnitude produced with the third algorithm presents a more regular trend. This is mainly due to the inclusion of a sort of low-pass filter implemented as a FIFO. A measure of its efficacy is obtained by evaluating the ratio between the standard deviation and the mean value of the signal – i.e. $s_2/m_2$ obtained by using the data of Figure 17.

This result is also confirmed by the frequency analysis (performed by using FFT) reported in Figures 15 and 16. In these figures, due to the stochastic nature of cavitation,
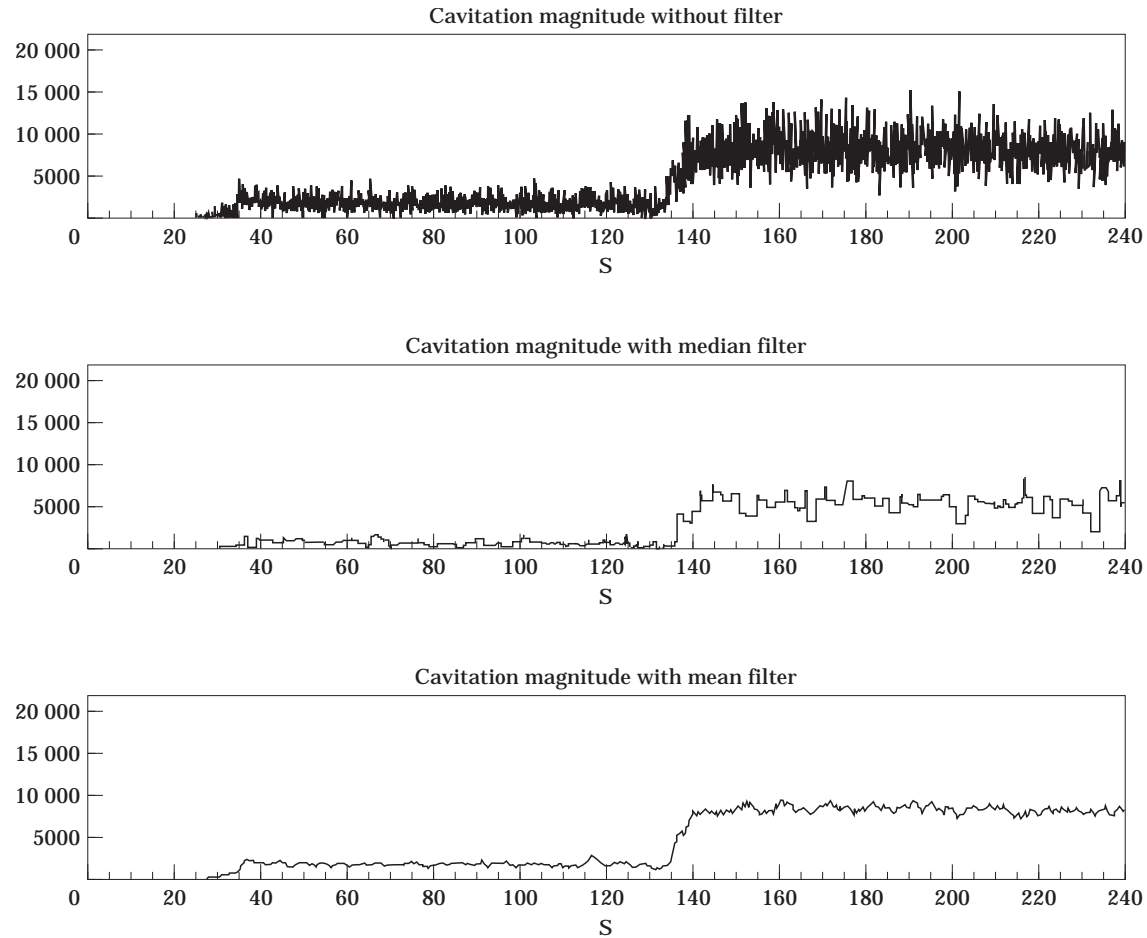
**Figure 12.** Cavitation magnitude as a function of time, obtained by using the second algorithm.

high-frequency components are present. The third algorithm offers the best immunity with respect to these components.
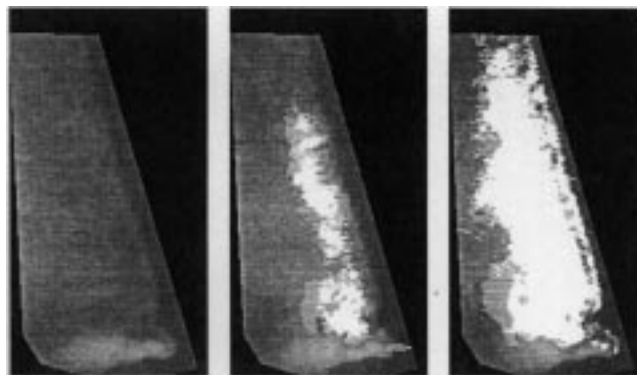
The performance which can be obtained by the algorithms proposed is directly related to the number of pixels which are present in the ROI. With a typical ROI of 27 762 pixels, the first and second algorithms are capable of processing 9.11 images per second (with filtering), while with the third algorithm only 7.52 images per second (without filter) are processed. Therefore, the first algorithm seems to be the best compromise between performance and quality with respect to the others, if the goal is the cavitation inception in real time. According to the linear dependence of estimation time with $R$ (the number of pixels in the ROI), the number of images processed per second can be easily increased by reducing $R$. On the other hand, the third algorithm is very interesting since it produces as an indirect result an image in which the cavitation area is well-identified (compare Figure 13 with respect to Figures 8 and 10 for the first and second
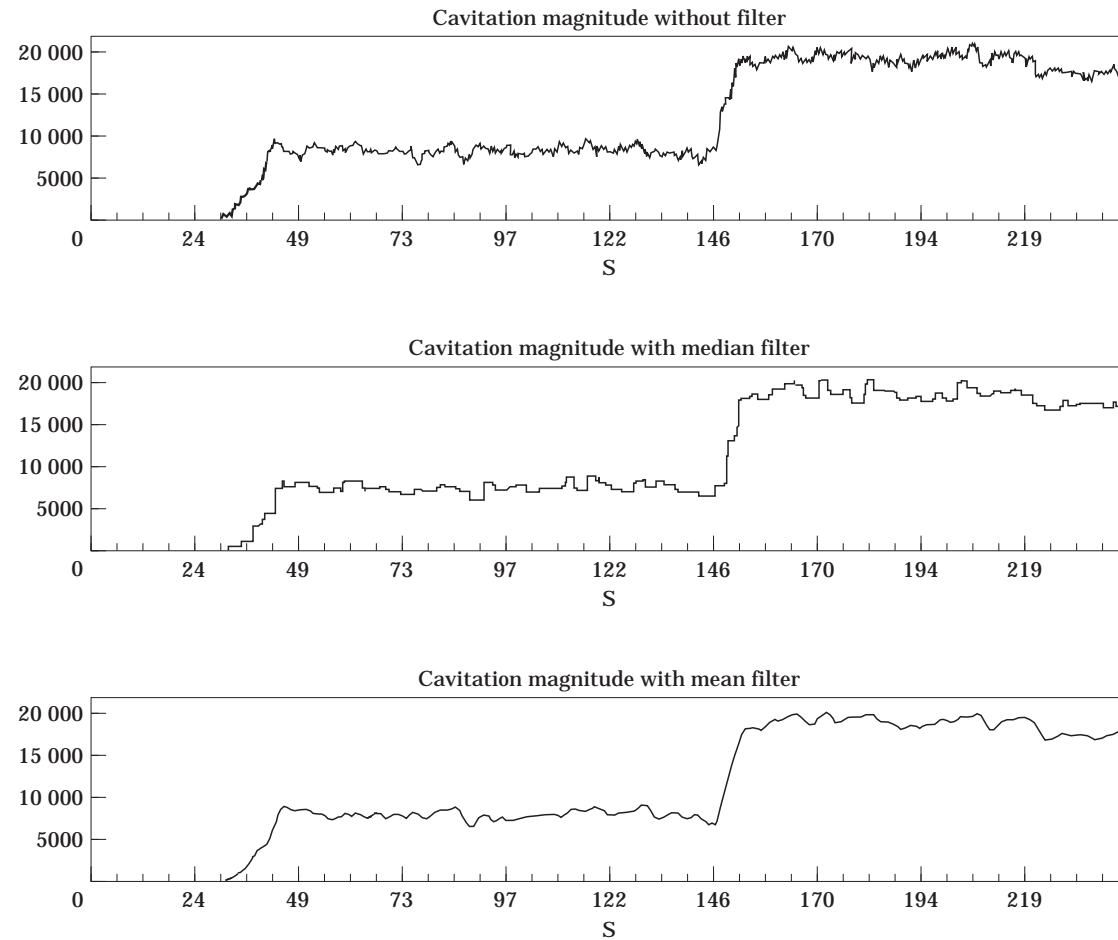


(a)  (b)  (c)

**Figure 13.** $A_c(\psi, \psi_r, th_c)$ set on frame during: (a) absence of cavitation ($t = 15$ s), (b) cavitation ($t = 75$ s), (c) strong cavitation ($t = 170$ s).

**Figure 14.** Cavitation magnitude as a function of time, obtained by using the third algorithm.
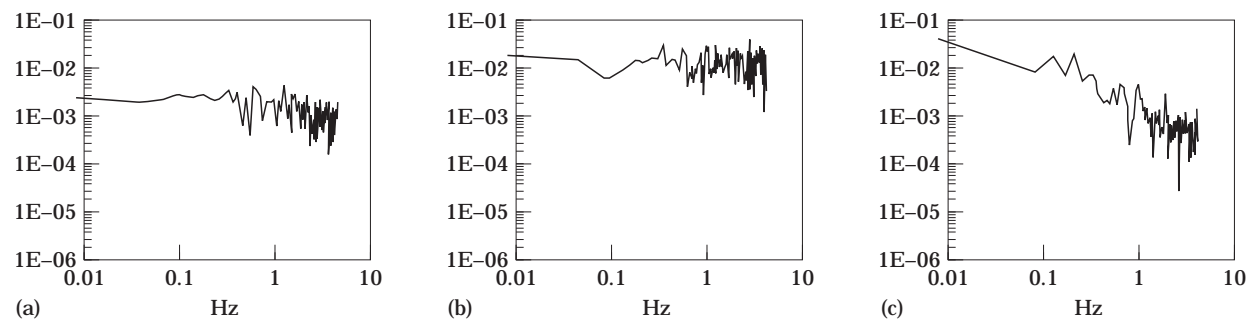


**Figure 15.** Normalized responses from the frequency analysis of the first algorithm for $f_a(t)$: (a) no cavitation without filtering; (b) cavitation without filtering; (c) cavitation with mean filtering.

algorithms). The image of $A_c(\psi, \psi_r, th_c)$ in Figure 13 has been suitably used for analysing cavitation conditions [16].

Moreover, it should be noted that the third algorithm has the worst performance on a general purpose machine, while it is more suitable for a hardware implementation than the other algorithms which have to perform mathematical operations for eliminating high frequency components. On the other hand, it needs a considerable memory space for storing a FIFO for each pixel.

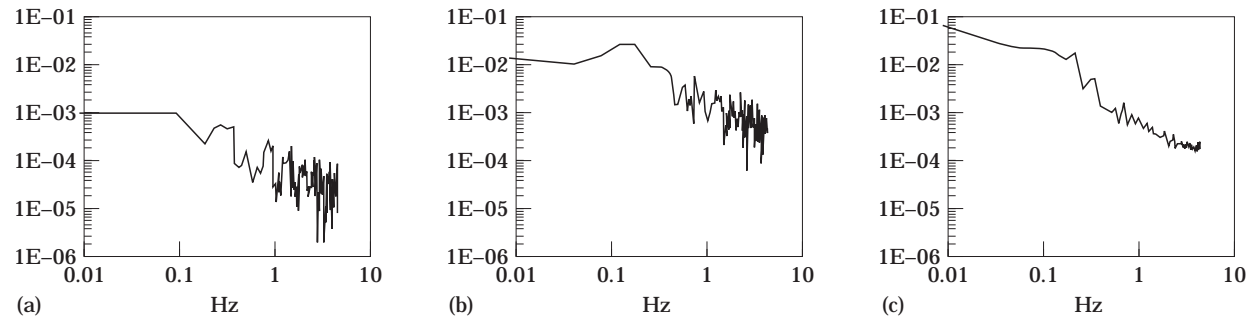In the literature, the cavitation phenomena is typically

**Figure 16.** Normalized responses from the frequency analysis of the third algorithm for $f_c(t)$: (a) no cavitation without filtering; (b) cavitation without filtering; (c) cavitation with mean filtering.

| Mean value | Without filter | | | With median filter | | | With mean filter | | |
|---|---|---|---|---|---|---|---|---|---|
| | $m_0$ | $m_1$ | $m_2$ | $m_0$ | $m_1$ | $m_2$ | $m_0$ | $m_1$ | $m_2$ |
| First algorithm | 1216 | 6777 | 16277 | 894 | 4349 | 13083 | 1155 | 6778 | 16210 |
| Second algorithm | 1.57 | 1792 | 8667 | 0 | 732 | 5619 | 1.13 | 1776 | 8555 |
| Third algorithm | 19 | 8153 | 19120 | 4.07 | 7591 | 18561 | 25 | 8072 | 19112 |

| Standard deviation | Without filter | | | With median filter | | | With mean filter | | |
|---|---|---|---|---|---|---|---|---|---|
| | $s_0$ | $s_1$ | $s_2$ | $s_0$ | $s_1$ | $s_2$ | $s_0$ | $s_1$ | $s_2$ |
| First algorithm | 166 | 1750 | 2096 | 411 | 735 | 1469 | 207 | 380 | 500 |
| Second algorithm | 7.08 | 858 | 2114 | 0 | 303 | 949 | 1.76 | 220 | 407 |
| Third algorithm | 23.5 | 548 | 1015 | 8.7 | 579 | 950 | 28 | 497 | 921 |

**Figure 17.** Mean values and standard deviation for the cavitation magnitude with and without filtering: $m_0$, $s_0$ in the absence of cavitation; $m_1$, $s_1$ during cavitation; $m_2$, $s_2$ during strong cavitation.

described in terms of relationship between the *pump head* and the net positive suction head (NPSH). The *pump head* is a measure of the specific work of the pump, while the NPSH is measured in meters of water column [12]. The NPSH factor is usually considered for measuring the distance from the current and the cavitation conditions.

In Figure 18 the behavior of pump head as a function of NPSH is reported for centrifugal pumps, where:

● $NPSH_{inc}$ = visual inception value, i.e. the condition in which the cavitation can be visually detected;
● $NPSH_{O\%}$ = value in which the cavitation becomes a problem for pump performance (in fact, after this value a decrease in pump head is detected);
● $NPSH_{1\%}$ = value in which the 1% head drop is measured;
● $NPSH_{fc}$ = value in which full cavitation or loss of performance is measured (in the impeller, there are large zones of fluid in both liquid and vapor phases).

Usually acoustic-based algorithms for cavitation detection must detect the vibrations on the machine. The vibrations, as a function of NPSH, present an evident spike between $NPSH_{0\%}$ and $NPSH_{1\%}$, as depicted in the work of

Gülich [12]; hence the effects of cavitation are relevant for performance pump. On the other hand, the algorithms proposed are capable of acting close to the $HPSH_{inc}$, which is very far from the $HPSH_{0\%}$ as described in Gülich [12], and verified by our experiments [16]. For this reason, the minimum level of cavitation inception that our algorithms can detect is strongly lower with respect to those provided by traditional techniques based on pressure measurement. In particular, from this point of view the third algorithm proves to be the best ranked among the algorithms pro-
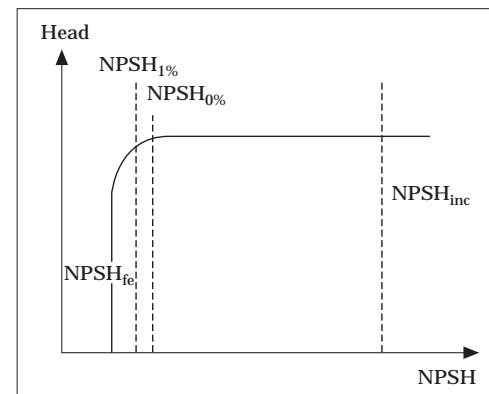


**Figure 18.** Pump head as a function of NPSH (typical behaviour).

posed. Moreover, all three algorithms are strongly robust with respect to detection of false negatives of cavitation, while some false negatives detecting cavitation inception can occur when threshold $td_x$ is too close to noise. This risk can be easily avoided by using higher threshold values, since for the cavitation considered in our experiments values of NPSH between $NPSH_{0\%}$ and $NPSH_{inc}$ were obtained for both the first and second levels of cavitation. This makes possible the increasing of threshold without problems, e.g. by making the threshold three times larger than the mean value of noise in the absence of cavitation.

## Conclusions

In this paper an image processing system for the real-time detection of cavitation inception was proposed. This technique can be applied on any hydraulic turbomachine, provided that an optical access is available. On the basis of this system three different algorithms have been defined, implemented and compared in real conditions. A real-time response was obtained, which ensures a high reliability of cavitation detection. One of these algorithms is also capable of producing results from which cavity length and extension can be directly evaluated, thus shortening the process of cavitation analysis.

## References

1. Stepanof, A.J. (1957) *Centrifugal and Axial Flow Pumps*. John Wiley & Sons.
2. Franc, J.P. *et al*. (1995) *La Cavitation, mécanismes physiques et aspects industrials*. Presses Universitaires de Grenoble.
3. Sulzer Brothers Ltd. (1989) *Sulzer centrifugal pump handbook*.
4. Lobanoff, V.S. & Ross, R.R. (1985) *Centrifugal pumps design & applications*. Gulf Publishing Company.
5. Foettinger, H. (1926) *Untersuchungen über Kavitation und Korrosion*. Hydraulicsche Probleme, Berlin, Verein Deutscher Ingenieure.
6. Canavelis, R. & Grison, P. (1986) Aspects industreles de la cavitation dans ies pompes. *Revue Française de Mecanique*, No. 4.
7. Durrer, H. (1986) *Cavitation Erosion and Fluid Mechanics*. Sulzer Technical review 3.
8. Varga, J.J., Sebestyen, G. & Fay, A. (1969) Detection of cavitation by acoustic and vibration-measurement methods. *La houille blanche*, No. 12.
9. Ceccio, S.L., Gowing, S. & Gindroz, B. (1995) A comparison of CSM bubble detection methods. *Cavitation and Gas-Liquid Flow in Fluid Machinery Devices*, ASME.
10. Merzkirsch, W. (1987) *Flow Visualization*. Academic Press.
11. Yang, We-Jei (1989) *Handbook of Flow Visualization*. Taylor & Francis.
12. Gülich, J.F. (1989) Guidelines for prevention of cavitation in centrifugal feedpumps. EPRI Report GS-6398.
13. Selim, S.M.A., Khalifa, B.A. & Hosien (1989) Cavitation inception in centrifugal pumps. *ASME Int. Symposium on Cavitation Inception*.
14. Vlaming, D.J. (1981) A method for estimating the net positive suction head required by centrifugal pumps. ASME Paper 81–WA/FE–32.
15. Stoffel, B. & Schuller, W. (1995) Investigations concerning the influence of pressure distribution and cavity length on the hydrodynamic cavitation intensity. *Cavitation and Gas-Liquid Flow in Fluid Machinery Devices*, ASME.
16. De Lucia, M. & Anguzza, G. (1994) Visualization and image processing to study the cavitation process in hydraulic turbomachinery. Modelling Testing & Monitoring for Hydro Powerplants, Conference Papers, The International Journal on Hydropower & DAMS, Budapest.
17. Arnone, A., Carnevale, E., De Lucia, M., Facchini, B. & Manfrida, G. (1991) Il banco prova del Dipartimento di Energetica dell'Università degli Studi di Firenze (DEF). *Proceedings 46 Congresso Nazionale A.T.I.*
18. Del Bimbo, A., Nesi, P. & Sanz, J.L.C. (1995) Analysis of optical flow constraints. *IEEE Transactions on Image Processing*, (4).
19. Pratt, W.K. (1978) *Digital Image Processing*. New York: John Wiley & Sons.